2020 IEEE/RSJ International Conference on Intelligent Robots and Systems (IROS)
October 25-29, 2020, Las Vegas, NV, USA (Virtual)

Robotic Micromanipulation of Biological Cells with Friction Force-Based Rotation Control

Shuai Cui and Wei Tech Ang

Abstract— **Cell manipulation is a critical procedure in related biological applications such as embryo biopsy and intracytoplasmic sperm injection (ICSI), where the biological cell is required to be oriented to the desired position. To bridge the gap between the techniques and the clinical applications, a robotic micromanipulation method, which utilizes friction forces to rotate the cell with standard micropipettes, is presented in this paper. Force models for both in-plane and out-of-plane rotations are well established and analyzed for the rotation control. For better controllability, calibration steps are also designed for adjusting the orientation of the micropipette with a more efficient way. A cell orientation recognition algorithm based on the superpixel segmentation and spectral clustering is reported and achieved high validation accuracy (96%) for estimating the orientation of the oocyte. The extracted visual information further facilitates the feedback control of cell rotation. Experimental results show that the overall success rate for the cell rotation control was about 95% with orientation precision of $\pm 1^{\circ}$.**

I. INTRODUCTION

Manipulation of a single biological cell is a fundamental process in several applications, such as pronuclear injection [1], embryo biopsy [2], and intracytoplasmic sperm injection (ICSI) [3]. These tasks all require the cell to be located precisely and rotated to the desired orientation. Over the last decade, related biological technologies have been widely developed and enabled continuous growth in the number of operations associated with cell manipulation. For example, the number of cycles involving preimplantation genetic diagnosis/screening (PGD/PGS) is keeping increasing [4]. Such growing demand imminently calls for the improvement of conventional cell manipulation techniques, which are performed manually with relatively low efficiency, poor dexterity, and weak reproducibility.

Multiple field-driven micromanipulation methods have been explored for manipulating biological cells. Optical tweezer can manipulate micro-objects like biological cells directly [5] or indirectly [6] through the force exerted by a strongly focused beam of laser. Acoustic tweezers control the rotation and translation of living cells through the acoustical radiation force with lower driving power compared to optical tweezers [7]. Induced by the dielectrophoresis, the electric torque was also taken to orient the suspended cells [8]. Although the aforementioned techniques have shown great potential in cell manipulation, there is still a wide gap between them and the practical applications. For instance, optical tweezer, as well as the acoustic tweezer, commonly are only capable of manipulating micro-objects within the two-dimensional space. Besides, the generated field may be detrimental to the target biological cells[9].

In standard fertility centers, cell manipulation, which usually refers to manipulating an embryo at the early developmental stage, is conducted by a pair of mechanical micromanipulators with appropriate micropipettes attached to it. In comparison with the field-driven methods, the operation may lack a certain amount of dexterity because of its limited degrees of freedom. However, it is superior in immobilizing and translating the cell with a larger force and higher stability. Therefore, automating the micromanipulation procedures carried out by the micropipette may provide an insight into improving the techniques for cell manipulation in relevant applications. A beveled injection micropipette can generate the rotation of an aspirated cell by poking into its surface with a certain depth [10], [11]. Although the risk of trauma brought by the sharp tip was reduced by minimizing the poking force, the weak control of the vacuum pressure for holding the cell may prevent the cell from rotating or cause it to escape from its fixed area. Friction force can also be directly utilized to rotate the cell. Aided by a mechanical device, the friction applied on the cell will drive it to rotate with the movement of the micropipette accordingly [12]. Nevertheless, in regards to the human or mouse oocyte, the width of the injection micropipette and the occlusion between it and the cell can not be neglected for the image processing and visual servo control.

A robotic cell manipulation method based on the friction force is proposed in this paper. Without any additional devices, the three-dimensional cell rotation is achieved purely with a pair of micropipettes and the substrate of the petri dish. Force models of the cell contacting with the holding micropipette, injection micropipette, and the substrate of the petri dish are developed to analyze how the friction applied on the cell is controlled to generate the desired rotation. Mouse oocyte is used for illustrating and validating the proposed method since it shares similar morphology and dimension with that of other mammalian animals. The cellular structure of the oocyte is clear without any interference during the whole process of rotation, which allows the polar body of the oocyte to be the feature indicating the orientation of the oocyte. The cell orientation recognition algorithm is designed on the basis of superpixel segmentation and spectral clustering analysis. As the success of the friction force-based cell manipulation highly relies on the alignment of the micropipettes, calibration steps for micropipettes are also designed.

S. Cui and W. T. Ang are with the school of Mechanical and Aerospace Engineering, Nanyang Technological University, 50 Nanyang Ave, 639798 Singapore. shuai002@e.ntu.edu.sg

978-1-7281-6211-9/20/$31.00 ©2020 IEEE

II. Experimental Setup

The robotic system is built on a motorized inverted microscope (Nikon, Eclipse Ti-U, Japan). As shown in Fig.1, other main components include a pair of 3-DOF mechanical micromanipulators (SM 3.25, Marzhauser Wetzlar), an X-Y linear translational stage (SCAN IM, Marzhauser Wetzlar), a holding micropipette (MPH-SM-45, Origio), an injection micropipette (MIC-35-30-B1.0, Origio), a CMOS camera (acA2040-90um, Basler), and a multi-channel motion controller (DMC 4183, Galil). The resolutions of the micromanipulator and the X-Y translational stage are 0.01μm and 0.025μm, respectively. Extra rotational degrees of freedom can be introduced by installing rotary motors on the 3-DOF micromanipulator, which will be used to adjust the orientation of the micropipette. The bending angles and the outer diameters of the holding and injection micropipette are 100μm, 8μm, 45°, 30°, respectively.

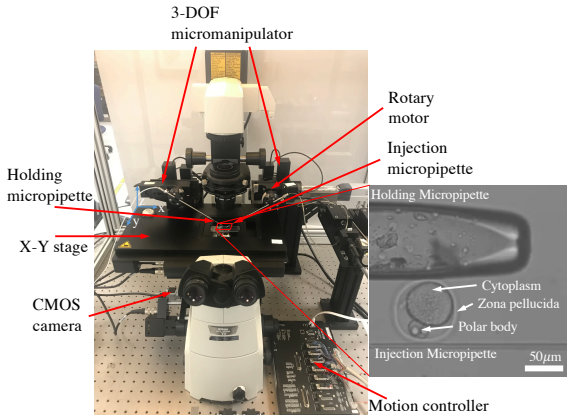

Fig. 1. Experimental setup with imaging system showing a scenario of the out-of-plane cell rotation

III. Friction Force-Based Cell Rotation Model

The model of the oocyte can be treated as a uniform elastic sphere in normal cases [13]. During the procedures of rotation control, the oocyte is immersed into the culture media with its motion controlled by a pair of micropipettes and the substrate.

A. Force Model for Out-of-Plane Rotation

The feature of the polar body may not be clearly visible under the microscope because of the self-occlusion or its defocused position. The task for the out-of-plane rotation is to rotate the oocyte and bring the polar body to the focal plane of the imaging system. Throughout the out-of-plane rotation, the micropipettes are held stationary while the frictions generating the rotation are produced by the movement of the substrate along the x-direction of the system. Fig. 2 shows the force model of a spherical oocyte during the out-of-plane rotation. The holding micropipette is lifted a certain height and presses on the surface of the oocyte together with the injection micropipette. The normal force between the oocyte and the holding micropipette has the component pointing downwards, which keeps a tight contact between the oocyte and the substrate. However, the angle between the y-axis and the line connecting the centers of the holding micropipette and the oocyte, β, has the maximum value to make sure that there is no interference between the holding micropipette and the inner cellular structure of the oocyte in the image frame. For this reason, we set the width of the blocking area $h = h_0$, as half of the width of the zona pellucida when the holding micropipette just touches the surface of the oocyte without any pressure. The value of β is obtained by:

$$cos\beta = \frac{R_H + R_C - h_0}{R_H + R_C} \tag{1}$$

where R_H and R_C are the radiuses of the holding micropipette and the oocyte, respectively.

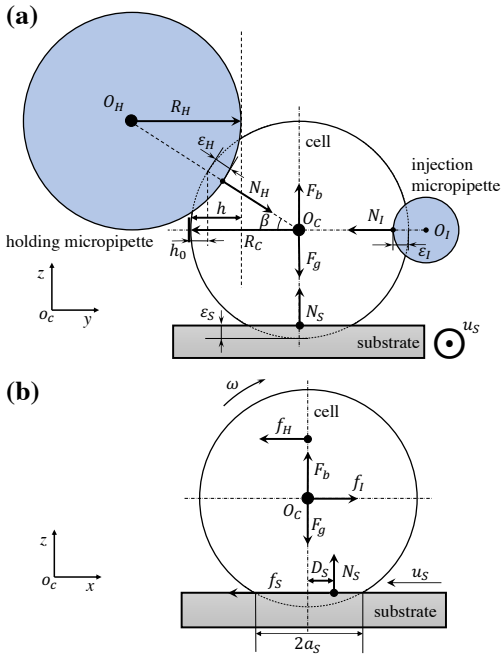

Fig. 2. Force model for the out-of-plane rotation in (a) yz plane, (b) xz plane.

The forces driving the rotation are mainly contributed by the frictions applied on the oocyte exerted by the holding micropipette and the substrate. The resistance torque between the oocyte and the injection micropipette is omitted on the basis of their much difference in size.

The oocyte has no relative motion or rotation in the yz plane. Thus, the forces applied on the oocyte are balanced as:

$$N_H cos\beta - N_I = 0 \tag{2}$$

$$N_S + F_b - N_H sin\beta - F_g = 0 \tag{3}$$

where N_H, N_I, and N_S are the normal forces between the oocyte and the holding, injection micropipettes, and the substrate, respectively; F_g and F_b are the gravity and buoyancy forces for the mouse oocyte.

Around the contact points, all the deformations are assumed to be totally elastic since they are small and local under the robotic control. The material of the micropipettes and the substrate is borosilicate glass, whose elastic modulus is many times larger than that of the mouse oocyte [10]. As a result, all the objects except the oocyte are treated as rigid bodies through the analysis. At the contact points between the oocyte and the micropipettes, the relationship between the normal force N and the compression ε on the oocyte is derived according to the Hertzian contact theory for the case of an elastic sphere contacting with a cylinder:

$$\varepsilon = K_1 \left[\frac{3(1-\upsilon_1{}^2)N}{2\pi E_1 \sqrt{K_2 R_C}} \right]^{\frac{2}{3}} \tag{4}$$

where υ_1 and E_1 are the Poisson's ratio and Young's Modulus of the oocyte, respectively; K_1, K_2 are constants determined by the dimensions of the oocyte and micropipettes, whose values can be acquired by referring to a given table in [14].

Similarly, the compression of the oocyte in contact with the substrate, ε_s, is also obtained from the case of a sphere in contact with a plane [15]:

$$\varepsilon_s = \left[\frac{3(N_I tan\beta + F_g - F_b)(E_1 + E_2 - \upsilon_2{}^2 E_1 - \upsilon_1{}^2 E_2)}{4E_1 E_2 \sqrt{R_C}} \right]^{\frac{2}{3}} \tag{5}$$

where υ_2 and E_2 are Poisson's ratio and the Young's modulus of the substrate, respectively.

Fig.2 (b) shows the out-of-plane rotation model in the xz plane. For an oocyte with mass of m, the relation between the resulting torque and its angular acceleration α is:

$$f_S(R_C - \varepsilon_S) - f_H(R_C - \varepsilon_H) sin\beta - N_S D_S = \frac{2mR_C^2\alpha}{5} \tag{6}$$

where D_s is the displacement of N_s, which is estimated about a quarter of the width of the contact region, $2a_S$; $\frac{2mR_C^2}{5}$ is the moment of inertia of the spherical oocyte; f_H is the friction between the oocyte and the holding micropipette, and f_S is the friction between the oocyte and the substrate. The frictions are proportional to the normal forces:

$$f_S = \mu_S N_S \quad \text{and} \quad f_H = \mu_H N_H \tag{7}$$

where μ_S and μ_H are the corresponding coefficients of f_S and f_H. Extremely large values of μ_S will definitely ensure the desired rotation of the oocyte while the particularly small ones may not be enough. Here we only consider about the most general scenario in practice as illustrated in Fig.2, where the value of μ_S is a little bit larger than that of μ_I.

B. Force Model for In-Plane Rotation

For the in-plane rotation, the holding micropipette is brought back to the focal plane, where the normal forces N_I and N_H are equal to each other. The oocyte will rotate with the moving micropipette until its desired orientation is reached. In the xy plane, the effects from the gravity and buoyancy forces are ignored. The force model for the in-plane rotation is shown in Fig.3.

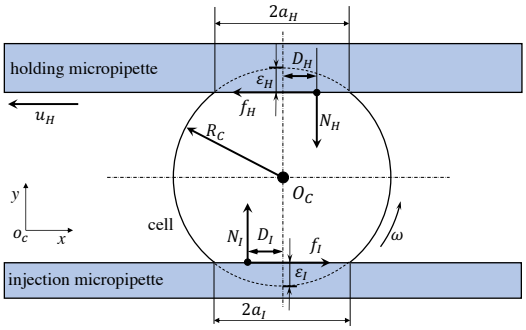

Fig. 3. Force model for the in-plane rotation.

Similarly, the relation between the resulting torque and the angular acceleration of the oocyte is:

$$f_H(2R_C - \varepsilon_I - \varepsilon_H) - N_I D_I - N_H D_H = \frac{7mR_C^2\alpha}{5} \tag{8}$$

where f_I is the friction applied on the oocyte in contact with the injection micropipette; D_I and D_H are the displacements of N_I and N_H during the rotation, respectively. The rotation axis is set on the surface of the injection micropipette.

C. Rotation Analysis

Along the y-direction of the micromanipulation system, adjusting the distance between the two micropipettes enables the fine control of the total compression on the oocyte ε_y.

$$\varepsilon_y = \varepsilon_I + \varepsilon_H cos\beta \tag{9}$$

The relationship between the angular acceleration α and the controlled compression ε_y is further analyzed with the derived models. The diameter of the oocyte is approximately 100μm, and its overall density is estimated as 1.08g/ml [16]. The density of water at 37°C is taken as the density of the culture media. The Poisson's ratios and Young's moduli of the oocyte and borosilicate glass are 0.5, 0.2, 15KPa, 63GPa, respectively. By looking up the table in [14], values of (K_1, K_2) for ε_I and ε_H are confirmed as (3.0889, 2.1171), and (1.9521, 1.0874), respectively. The angle of β is around 11.48°, in accordance with the value of h_0 set as 2μm. The reference values of the coefficients (μ_I, μ_H, μ_S) are reasonably assumed to be (0.15, 0.05, 0.16) [10]. As the surface of the micropipettes is well polished, μ_S is set a little bit higher than μ_I.

By substituting (2), (9) into (4), we obtain that $\varepsilon_I = 1.25\varepsilon_H$, and $\varepsilon_I = 1.26\varepsilon_H$ under the circumstances of out-plane-rotation and in-plane rotation, respectively. Given with a known ε_y, the corresponding values of the compressions ε_I, ε_H, ε_S and the normal forces N_I, N_H, N_S are calculated using (2), (3), (4), and (5). Then from (6) and (8), the corresponding angular accelerations α with the varying values of ε_y are computed under the circumstances of out-of-plane and in-plane rotation, respectively [see Fig. 4]. The results show that an effective rotation only happens when the value of ε_y is less than 12.0μm for the out-of-plane rotation and 0.55μm for the in-plane rotation. Within the effective range of ε_y, the large positive angular acceleration implies that the acceleration

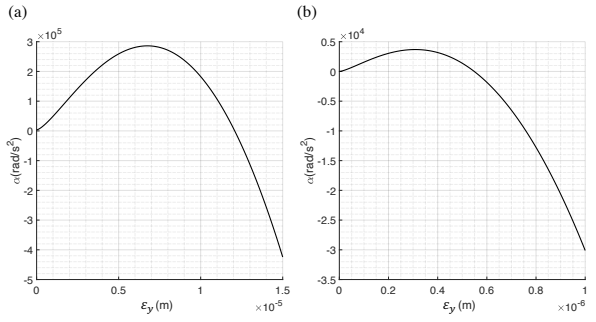

Fig. 4. The angular acceleration α of the oocyte with the varying values of its total compression along the y-direction, ε_y, in the case of (a) out-of-plane rotation, (b) in-plane rotation.

process is instantaneous for the static oocyte to catch up the velocity of the substrate or the moving micropipette. In fact, real oocytes are not perfect spheres even their ellipticity are small. If the value of ε_y is chosen as too small, the surface of the oocyte may detach from the micropipette through the process of rotation. Intuitively, the micropipettes should be pressed more firmly on the oocyte. However, as it is shown in Fig. 4, the rotation will not be generated when the compression ε_y lies outside of the effective range with the negative angular acceleration. Compared to the out-of-plane rotation, the in-plane rotation has much narrower room to adjust the compression applied on the oocyte, which means that the micropipette should be finely oriented and aligned before the cell rotation control.

IV. Vision Guided Cell Rotation Control

A. Micropipette Orientation Calibration

As it is discussed in Section III, the orientation of the micropipette must be well calibrated and aligned with the coordinates of the system to initialize the cell rotation control. A micropipette is inserted to a holder which is attached to the micromanipulator. The end part of the micropipette is bent with a certain bending angle ($20^\circ \sim 45^\circ$) to manipulate suspended cells. Consequently, the angle ψ_2, with which the holder is held should be equal to the bending angle to ensure that the bent part is parallel to the xy plane. Although it is fixed on the micromanipulator, the holder can rotate freely around its own axis, resulting that the micropipette may have different orientations ψ_1 in the image frame [see Fig. 5(a)]. Given the above, the micropipette orientation calibration is concluded as a task to adjust the micropipette until its bent part is in parallel with both the x-axis and xy plane. The holding micropipette mounted on the left side of the microscope is taken for illustration. When installing the micropipette holder on the micromanipulator, the tip-end of the micropipette is able to be manually positioned at the fourth quadrant (micropipettes on the left side) pointing upwards without too much effort [see Fig. 5(b)].

The information of the orientation ψ_1 can be directly extracted from the image. As shown in Fig. 5(a), a micropipette always has the regular shape and sharp edges in its focused image plane. By applying an edge detection algorithm along with the morphological operators, the outline of the micropipette shall be easily separated from the background. To further get the accurate orientation estimation, we applied the method depicted in [17]. By averaging the orientations estimated at each local point along the edge of the micropipette, the value of ψ_1 is acquired, which will guide the controller to rotate the holder around its own axis and align the micropipette with the x-axis in the image plane.

Unlike ψ_1, the inclined angle ψ_2 of the holder cannot be read directly from the image. Some of the micromanipulators may have the circular dial scale as the assistance for rotating the holder. However, the installation error may still lead to an unreliable result. Here, we propose an efficient calibration method with the reference information from the imaging system and the controller. Fig. 5(b) shows the geometric relationship when the holder rotates with the rotary motor.

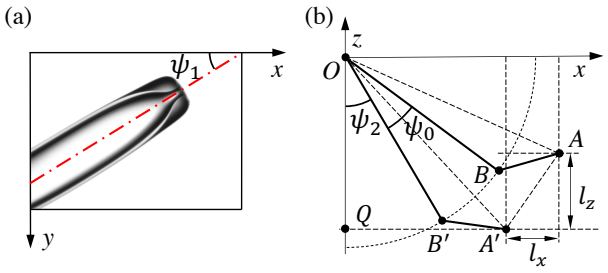

Fig. 5. (a) Micropipette orientation in the image plane. (b) Geometrical model of a rotating micropipette. Point O is the center of rotation on the axis of the holder. Line segment AB represents the bent part of the micropipette with its tip-end labeled as A. The ratio between AB and OB is exaggerated in the diagram. $A'B'$ is the bent part after being rotated.

The calibration steps are designed as follows:

a) Get the most focused image frame for the tip-end
b) Record the position of the tip-end in the image frame and the depth of the focal plane
c) Rotate the micropipette holder clockwise with a certain angle ψ_0 by the rotary motor
d) Update the most focused image frame for the tip-end
e) Record the new position of the tip-end in the imaging frame and the updated depth of the focal plane
f) Get the relative displacements of the tip-end along the x, z-directions and convert them to the length of l_x, l_y, respectively

Sometimes the tip-end is out of the field of view after the rotation. In such case, the motion controller will bring it back along the x-direction and move it to the same position in the focused image frame before it was rotated. Then the value of l_x will be obtained from the reference information provided by the motion controller. The inclined angle after the rotation is estimated as:

$$\psi_2 \approx \angle QOA' = \frac{\pi - \psi_0}{2} - tan^{-1}\frac{l_x}{l_z} \tag{10}$$

With the known value of ψ_2, the rotary motor will adjust the holder to the right orientation where the inclined angle is consistent with the bending angle.

It should be noticed that the diagram in Fig. 5(b) is exaggerated for demonstration. In fact, the bent part of the micropipette is only 1mm or even shorter, whose length can be ignored compared to the distance between the center of rotation and the micropipette tip-end (approximately13cm). In the case with the bending angle of 30°, $\angle AOB$ is about 0.22°, which causes the height difference along the bent part around 4μm. Therefore, the alignment algorithm has sufficient precision and is fully acceptable for our work.

B. Cell Orientation Recognition

As the feature indicating the orientation of the oocyte, polar body detection is essential for the cell rotation control. Traditional techniques employed to identify the cellular structure mainly include edge detection [13], morphological operators [18], and etc. While efficient, these methods may encounter difficulties with inconsistent results emerging from cases under different light conditions, image contrast, and resolutions. Recently, neural networks are adopted in detecting the presence of the polar body as its performance has been well recognized in dealing with object detection tasks in the macro world [11]. Nevertheless, neural networks are not applicable in most of the real-time micromanipulation system currently due to their higher computational consumption.

According to our cell manipulation method, the oocyte does not remain fixed during the procedures of rotation. To provide a wider field of view, a 10× objective lens is chosen for the imaging system to monitor the motion of the oocyte. Within the image frame, the region of the oocyte is located by the Lucas-Kanade template tracking algorithm [19]. The template is set to have the size of 256×256 pixels, which allows the entire oocyte to be incorporated and centered in the frame. However, the image patches of the oocyte provided by the 10× objective lens may still have some blurry boundaries. To address this challenge, a cell orientation recognition algorithm is proposed based on the split and merge strategy. An image patch of the oocyte is first divided into many uniform superpixels, which reduces the computational complexity but keeps the necessary information for further analysis. Subsequently, the superpixels will be merged and grow until the complete contour of the oocyte appears.

Generating the superpixel has been attempted by many approaches. In this work, the framework of simple linear iterative clustering (SLIC) is implemented, with which the output superpixels have relatively regular size and shape [20]. Fig. 6(b) shows the oversegmentation result of the sample oocyte image, where the superpixel are with the size of 8×8 pixels. The generated superpixels are then merged to create the desired segmented result. The merging process generally has two steps. (1) Merge the superpixels into larger clusters. (2) Merge the clusters into two regions, which are with, or without the polar body in combination with the cytoplasm. Since spectral clustering outscores other clustering analysis techniques such as K-means, density-based methods with better robustness, adaptability, and computational efficiency, it is selected to realize the first step.

Given a grayscale image patch containing the oocyte with the frame size of H×W, the distance between the ith and jth superpixels, SP_i and SP_j, can be measured as:

$$d_{ij} = \sqrt{(I_i - I_j)^2 + \frac{1}{\eta^2 HW}[(x_i - x_j)^2 + (y_i - y_j)^2]} \quad (11)$$

where I_i, I_j are the mean pixel intensities of SP_i and SP_j, with centroids at points of (x_i, y_i) and (x_j, y_j), respectively; η is a scaling factor, which tunes the effect of the planar position in the evaluation of the distance between two superpixels.

With n superpixels generated, the similarity matrix $S = (s_{ij})_{i,j=1\ldots n}$ is defined as:

$$s_{ij} = \begin{cases} \exp\left(\frac{-d_{ij}^2}{2\sigma_i\sigma_j}\right) & \text{, if } i \in kNN_j \text{ or } j \in kNN_i \\ 0 & \text{, otherwise} \end{cases} \quad (12)$$

where σ_i and σ_j are the local scales, with $\sigma_i = \sum_{l \in kNN_i} \frac{d_{il}}{k}$; kNN_i and kNN_j are the index sets of k nearest neighbors of SP_i and SP_j , respectively.

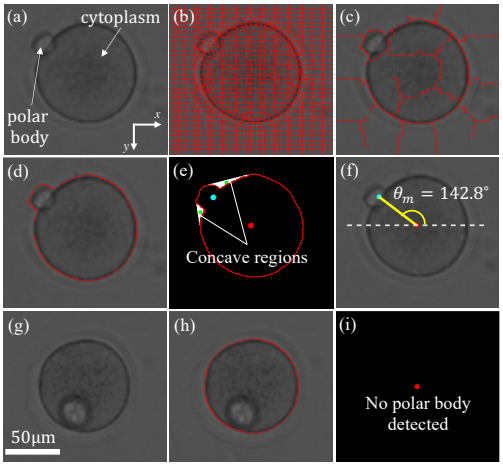

Fig. 6. Orientation recognition for a mouse oocyte. (a) Focused image of the oocyte with the polar body close to the focal plane. (b) Oversegmentation result with superpixels. (c) Merging superpixels with the spectral clustering. (d) Segmentation result of the intracellular structure. (e) Concave regions displayed in a binary image by subtracting the intracellular structure from its convex hull. The red point represents the centroid of the intracellular structure while the cyan point indicates the position of the polar body (f) Orientation of the oocyte (g) Case with the polar body at a depth away from the focal plane. (h) Segmentation result. (i) No polar body detected.

Fig. 6(c) shows the spectral clustering result of the sample image ($H = W = 256$, $k = 7$, and $\eta = 0.01$). These clusters will be further merged until the contour of the intracellular structure clearly appears. The merging criterion is based on the Bhattacharyya distance between every two clusters. After every cluster has fully grown, clusters whose boundaries overlap with the image borders will be assigned with the same label; and the rest parts of the image are treated as the intracellular structure, which is a combo of the polar body and the cytoplasm [see Fig. 6(d)].

The orientation of an oocyte is typically estimated by the relative position between the polar body and cytoplasm. With the polar position of the polar body to the cytoplasm,

the set of points inside the boundary of the intracellular structure is non-convex. The concave regions are obtained by subtracting the intracellular structure from its convex hull. To suppress the error and undesired regions caused by the jagged edges, the morphological operation of erosion is also performed. The subtraction result of the sample image, including the two concave regions, is shown in Fig. 6(e). The geometric center of the two concave regions (for oocyte with a single polar body) on the plane is then considered as the position of the polar body. By calculating the slope of the line connecting the centroid of the cellular structure and the indicated position of the polar body, the orientation of the oocyte is well detected as shown in Fig. 6(f).

C. Control Strategy

The robotic micromanipulation system for the cell rotation control is summarized in Fig. 7. The rotation mode is switchable depending on the detected orientation of the oocyte. Adjusting the alignment of the micropipette is also integrated in the system. As it indicates in Section III, the varying elastic compression of the oocyte along the y-direction, ε_y, determines whether the oocyte can be rotated or not. To ensure the controllability of the manipulation, the system requests that the micropipettes should be well aligned every time the rotation is about to be initialized or just switched between the two modes.

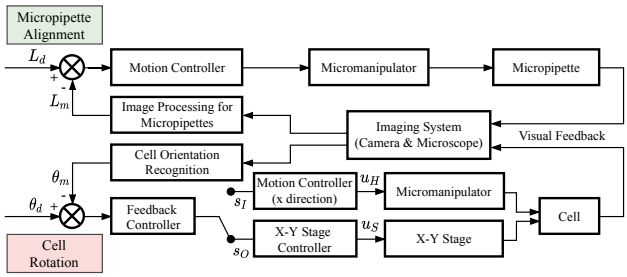

Fig. 7. Diagram for the cell rotation control system. s_I and s_O are the switches between the modes of in-plane and out-of-plane rotations. L_d and θ_d are the desired position and orientation of the micropipettes and the oocyte, respectively; L_m and θ_m are the measured ones. u_H, u_S are the velocities of the holding micropipette and the substrate along the x-direction.

The out-of-plane rotation starts with the substrate moving along the x-direction and terminates when the presence of the polar body is identified. As the polar body gets closer to the focal plane during the rotation, the total area of the concave regions, A (pixels), will keep increasing until it reaches to the peak value. Therefore, the termination condition of the out-of-plane rotation is met when the total area of the concave regions is larger than the threshold value, A_t (pixels). For the substrate, a piecewise proportional controller is designed with the gain of k_{po} [21]:

$$u_S = \begin{cases} 5\mu\text{m}/s & \text{if} \quad A = 0 \\ k_{po}(A_t - A) & \text{if} \quad 0 < A \le A_t \\ 0 & \text{if} \quad A > A_t,\ A(i-1) \le A(i) \\ -5\mu\text{m}/s & \text{if} \quad A > A_t,\ A(i-1) > A(i) \end{cases} \tag{13}$$

The control system will switch to the mode of in-plane rotation once the out-of-plane rotation is done. The holding micropipette moves back to the focal plane and drives the oocyte to rotate to the desired orientation θ_d with its movement along the x-direction. The real-time orientation of the oocyte θ_m is measured by the visual recognition algorithm. With the difference between the θ_d and θ_m as the input, the velocity of the moving holding micropipette is controlled by a PD controller:

$$u_H = k_p(\theta^d - \theta^m) - k_d\dot{\theta}_m \tag{14}$$

where k_p and k_d are the proportional and derivative gains, respectively. A demo of the system manipulating the mouse oocyte with rotation control is presented in the attached video.

V. Experimental Results and Discussion

A batch of 50 mouse oocytes was collected for evaluating the proposed cell rotation method and the orientation recognition algorithm. Ten of the oocytes were used to confirm the optimal values of the undetermined parameters. The rest oocytes were divided into two parts. The in-plane and out-of-plane rotation were tested on the first 20 oocytes independently. With the last 20 oocytes, the system was asked to execute the two modes of rotation consecutively and orient the oocyte to the desired orientation. For each oocyte, two frames were captured from its off-line videos for validating the cell orientation recognition algorithm. The oocytes were immersed in the culture media and placed on a heating plate with the temperature of 37°C through the operations. The effective ranges of the compression ε_y were empirically obtained as $0 \sim 9.0 \pm 1\mu$m and $0 \sim 0.6 \pm 0.2\mu$m for the out-of-plane and in-plane rotation, respectively. An optimal value for the threshold area of A_t was found about 496 (pixels) with the pixel resolution of 0.67μm/pixel. The gains for the feedback controller were tuned as $k_{po} = 0.02$, $k_p = 0.56$, $k_d = 0.11$ with the angle in rad/s and the velocity of the moving micropipette in μm/s.

A. Cell Orientation Recognition

The orientation of the cell in each frame was calculated manually as the ground truth. Since the shape of the polar body in the oocyte could be irregular or asymmetric, the orientation detected from the proposed algorithm might have large disparity from the result which was calculated manually. The measured orientation θ_m was considered as correct if the error was within $\pm 5^\circ$. The experimental result showed that the algorithm successfully detected the orientation of the oocyte on 96 frames, with which the success rate was 96%.

B. Cell Rotation Control

Cell rotation test began with the out-of-plane rotation on the first 20 oocytes. A successful out-of-plane rotation required the polar body to be brought close to the focal plane in a steady state. The oocyte was randomly rotated before each trial of the rotation. With 5 trials on each oocyte, the polar body of the oocyte was successfully brought to the focal plane 93 times. All the failed attempts fell on the two

oocytes, whose cytoplasm shrank obviously due to the long time exposure to the outside environment.

In the experiments for the in-plane rotation, each oocyte was first rotated to the 9 o'clock direction manually. The angle was measured and recorded as the ground truth with the orientation recognition algorithm. Then the oocyte was required to be rotated back to the 9 o'clock position after being randomly rotated within the *xy* plane. The process was repeated 5 times for each oocyte. The overall success rate was 95% with angular precision of $\pm 1^{\circ}$. The oocytes in the failed trials had large ellipticity in common, which caused inevitable slippage during the operation.

The overall performance of the micromanipulation system was finally assessed with another 20 oocytes. The system was set to orient the polar body to the 6 o'clock position without any manual interruptions between the out-of-plane and the in-plane rotation. Out of the 20 oocytes, the one-time success rate reached to 95%. For the failed one, the oocyte had a notch on the cytoplasm, which made the system confused to find out the accurate orientation of the oocyte.

C. Discussion

The algorithm for detecting the orientation of the cell was derived in the case with only one polar body exists. However, it is robust in dealing with situations that the polar body has variations on the features of number, size, and shape. For example, if there are two polar bodies seen in the oocyte, the detected position indicating by the algorithm will locate somewhere between the two polar bodies. As long as the polar bodies do not depart too far away with each other, the recognition results are reasonable in the real applications.

Although parts of the force model were built on assumptions, cell rotation control was successfully achieved by the system in combination with the experience gained from the tests and the directions pointed by the theoretical model.

VI. CONCLUSIONS

A friction force-based cell rotation method was illustrated and modeled with analysis in this paper. By fine adjusting the elastic compression applied on the oocyte, corresponding rotations were generated with the moving micropipette or the substrate. To realize the robotic cell manipulation, a vision guided control system was designed and validated on the model of mouse oocytes. Through the tests, the embedded visual algorithm achieved an accuracy of 96% in recognizing the orientation of the oocyte. Overall success rate reached to 95% in the cell orientation control with precision of $\pm 1^{\circ}$. The experiments results well suggested the feasibility of the proposed methods and the designed system, which may contribute to the related biological applications in the future.

REFERENCES

[1] L. M. Ittner and J. Götz, "Pronuclear injection for the production of transgenic mice," *Nature protocols*, vol. 2, no. 5, p. 1206, 2007.

[2] M. Montag, K. Van der Ven, B. Rösing, and H. Van der Ven, "Polar body biopsy: a viable alternative to preimplantation genetic diagnosis and screening," *Reproductive biomedicine online*, vol. 18, pp. 6–11, 2009.

[3] L. Van der Westerlaken, F. Helmerhorst, J. Hermans, and N. Naaktgeboren, "Intracytoplasmic sperm injection: position of the polar body affects pregnancy rate," *Human Reproduction*, vol. 14, no. 10, pp. 2565–2569, 1999.

[4] J. C. Harper, L. Wilton, J. Traeger-Synodinos, V. Goossens, C. Moutou, S. SenGupta, T. Pehlivan Budak, P. Renwick, M. De Rycke, J. Geraedts, *et al.*, "The eshre pgd consortium: 10 years of data collection," *Human reproduction update*, vol. 18, no. 3, pp. 234–247, 2012.

[5] M. Xie, J. K. Mills, Y. Wang, M. Mahmoodi, and D. Sun, "Automated translational and rotational control of biological cells with a robot-aided optical tweezers manipulation system," *IEEE Transactions on Automation Science and Engineering*, vol. 13, no. 2, pp. 543–551, 2015.

[6] A. Thakur, S. Chowdhury, P. Švec, C. Wang, W. Losert, and S. K. Gupta, "Indirect pushing based automated micromanipulation of biological cells using optical tweezers," *The International Journal of Robotics Research*, vol. 33, no. 8, pp. 1098–1111, 2014.

[7] I. Bernard, A. A. Doinikov, P. Marmottant, D. Rabaud, C. Poulain, and P. Thibault, "Controlled rotation and translation of spherical particles or living cells by surface acoustic waves," *Lab on a Chip*, vol. 17, no. 14, pp. 2470–2480, 2017.

[8] P. Benhal, J. G. Chase, P. Gaynor, B. Oback, and W. Wang, "Ac electric field induced dipole-based on-chip 3d cell rotation," *Lab on a Chip*, vol. 14, no. 15, pp. 2717–2727, 2014.

[9] J. L. Sebastián, S. Muñoz, M. Sancho, G. Martínez, and G. Álvarez, "Electromechanical effects on multilayered cells in nonuniform rotating fields," *Physical Review E*, vol. 84, no. 1, p. 011926, 2011.

[10] Q. Zhao, M. Sun, M. Cui, J. Yu, Y. Qin, and X. Zhao, "Robotic cell rotation based on the minimum rotation force," *IEEE Transactions on Automation Science and Engineering*, vol. 12, no. 4, pp. 1504–1515, 2014.

[11] C. Dai, Z. Zhang, Y. Lu, G. Shan, X. Wang, Q. Zhao, and Y. Sun, "Robotic orientation control of deformable cells," in *2019 International Conference on Robotics and Automation (ICRA)*. IEEE, 2019, pp. 8980–8985.

[12] Z. Wang, C. Feng, R. Muruganandam, W. T. Ang, S. Y. M. Tan, and W. T. Latt, "Three-dimensional cell rotation with fluidic flow-controlled cell manipulating device," *IEEE/ASME Transactions on Mechatronics*, vol. 21, no. 4, pp. 1995–2003, 2016.

[13] I. A. Ajamieh, B. Benhabib, and J. K. Mills, "Automatic system for the blastocyst embryo manipulation and rotation," *Annals of biomedical engineering*, vol. 48, no. 1, pp. 426–436, 2020.

[14] M. Puttock, E. Thwaite, *et al.*, *Elastic compression of spheres and cylinders at point and line contact*. Commonwealth Scientific and Industrial Research Organization Melbourne ..., 1969.

[15] Z. Wang, W. T. Latt, S. Y. M. Tan, and W. T. Ang, "Visual servoed three-dimensional cell rotation system," *IEEE Transactions on Biomedical Engineering*, vol. 62, no. 10, pp. 2498–2507, 2015.

[16] W. H. Grover, A. K. Bryan, M. Diez-Silva, S. Suresh, J. M. Higgins, and S. R. Manalis, "Measuring single-cell density," *Proceedings of the National Academy of Sciences*, vol. 108, no. 27, pp. 10 992–10 996, 2011.

[17] C. Y. Wong and J. K. Mills, "Cleavage-stage embryo rotation tracking and automated micropipette control: Towards automated single cell manipulation," in *2016 IEEE/RSJ International Conference on Intelligent Robots and Systems (IROS)*. IEEE, 2016, pp. 2351–2356.

[18] Z. Wang, C. Feng, W. T. Ang, S. Y. M. Tan, and W. T. Latt, "Autofocusing and polar body detection in automated cell manipulation," *IEEE Transactions on Biomedical Engineering*, vol. 64, no. 5, pp. 1099–1105, 2016.

[19] S. Baker and I. Matthews, "Lucas-kanade 20 years on: A unifying framework," *International journal of computer vision*, vol. 56, no. 3, pp. 221–255, 2004.

[20] R. Achanta, A. Shaji, K. Smith, A. Lucchi, P. Fua, and S. Süsstrunk, "Slic superpixels compared to state-of-the-art superpixel methods," *IEEE transactions on pattern analysis and machine intelligence*, vol. 34, no. 11, pp. 2274–2282, 2012.

[21] C. Leung, Z. Lu, X. P. Zhang, and Y. Sun, "Three-dimensional rotation of mouse embryos," *IEEE Transactions on Biomedical Engineering*, vol. 59, no. 4, pp. 1049–1056, 2012.